INORGANIC CHEMISTRY FRONTIERS

RESEARCH ARTICLE

View Article Online
View Journal | View Issue

Cite this: *Inorg. Chem. Front.*, 2025, **12**, 4019

Ligand-driven facet control of InAs-based quantum dots for enhanced near- and shortwave infrared emission†

Hyunjin Cho,[a] Yujin Kim,[a] Whi Dong Kim,[b,c] Young-Shin Park,[d] Ju Young Woo, *[c,e,f] Hyung-Kyu Lim *[g] and Doh C. Lee *[a]

InAs-based quantum dots (QDs) are promising heavy-metal-free semiconductors for infrared emission technologies, offering tunable bandgaps *via* quantum confinement and excellent charge-carrier transport properties. Building on these advantages, we report the synthesis of QDs tailored for emission in the near-infrared (NIR) and short-wave infrared (SWIR) regions, emphasizing the critical role of capping ligands in controlling surface facet populations and nanocrystal morphology. Specifically, we demonstrate that the choice of ligand plays a critical role in determining the morphology and surface characteristics of InAs QDs. Using dioctylamine as a ligand results in InAs QDs with a spherical or tetrapod morphology, where nonpolar (110) facets are predominantly exposed on the surface. In contrast, oleic acid as a ligand promotes the formation of tetrahedral-shaped QDs with polar (111) crystalline planes being more prominently exposed. Using a one-pot synthesis approach, we successfully synthesized InAs/InZnP/ZnSe/ZnS core-multi-shell structures that effectively minimize interfacial defects. QDs with dioctylamine-capped core exhibit significantly higher photoluminescence quantum yield (PLQY) compared to those with oleic acid-capped cores. We achieved a PLQY of 39% at 1260 nm and 7.3% at 1420 nm with QDs using dioctylamine, representing efficiency values among the best reported in both the NIR and SWIR regions. Transient absorption (TA) spectroscopy reveals that dioctylamine-capped QDs exhibit reduced ground-state bleaching differences across excitation wavelengths compared to oleic acid-capped QDs, indicating significantly reduced interfacial trap states. These findings highlight the importance of ligand-driven facet control in the context of minimizing interfacial defect formation.

Received 16th January 2025,
Accepted 25th March 2025

DOI: 10.1039/d5qi00142k

rsc.li/frontiers-inorganic

Introduction

Infrared (IR) light, which extends beyond the visible spectrum, is broadly classified into specific wavelength regions. Among these, near-infrared (NIR, 750–1400 nm) and short-wave infrared (SWIR, 1400–3000 nm) regions are particularly important due to their various applications in optical sensing, including facial recognition, autonomous vehicle vision systems, bioimaging, and free-space optical communication.[1–10] However, current manufacturing processes are limited by high costs and low productivity, primarily due to the need for high-temperature epitaxial growth. Solution-based processes, particularly those utilizing colloidal quantum dots (QDs), offer a promising alternative by enabling large-scale production at lower temperatures with reduced costs[7,11–17] These QDs offer unique advantages by enabling precise tuning of absorption and emission wavelengths, extending into the infrared range. Specifically, semiconductors such as PbS, PbSe, and InAs can be engineered into QDs with tailored optical properties targeting distinct infrared regions, including NIR and SWIR, thereby expanding their potential applications.

InAs QDs represent a promising non-toxic alternative to Pb-based materials, distinguished by their superior electronic properties including high electron mobility, low exciton binding energy, and large exciton Bohr radius.[18–24] These character-

[a]*Department of Chemical and Biomolecular Engineering, Energy and Environmental Research Center (EERC), KAIST Institute for NanoCentury (KINC), Korea Advanced Institute of Science and Technology (KAIST), Daejeon 34141, Republic of Korea. E-mail: dclee@kaist.edu*
[b]*Carbon Neutral Technology R&D Department, Korea Institute of Industrial Technology (KITECH), Cheonan 31056, Republic of Korea*
[c]*Autonomous Manufacturing and Process Department, KITECH, Ansan 15588, Republic of Korea. E-mail: jywoo@kitech.re.kr*
[d]*Chemistry Division, Los Alamos National Laboratory, Los Alamos, New Mexico 87545, USA*
[e]*School of Integrative Engineering, Chung-Ang University, Seoul 06974, Republic of Korea*
[f]*HYU-KITECH Joint Department, Hanyang University, Ansan 15588, Republic of Korea*
[g]*Division of Chemical Engineering and Bioengineering, Kangwon National University, Chuncheon, 24341, Republic of Korea. E-mail: hklim@kangwon.ac.kr*
† Electronic supplementary information (ESI) available. See DOI: https://doi.org/10.1039/d5qi00142k

istics make them particularly suitable for infrared emission applications. However, a significant challenge emerges as the QD core size increases: the growth of QDs into less homogeneous size and shape and the formation of interfacial defects at the core/shell interface leads to substantial decrease in photoluminescence quantum yield (PLQY), a phenomenon particularly pronounced in InAs-based QDs.[25–27] While recent studies have employed Cd-containing shells to address the lattice mismatch issue to reduce interfacial strain, the inherent toxicity of Cd-based materials presents persistent environmental challenges.[21]

To address these challenges, this study introduces a novel approach utilizing ligand-driven facet control during core growth to mitigate interfacial defect formation and improve emission efficiency of larger InAs QDs without relying on toxic materials. This strategy highlights the fundamental role of ligand adsorption in shaping QD morphology and facet exposure, as changes in the facets can alter the distribution of dangling bonds, which in turn affects the formation of interfacial defects. The exposure of specific facets can lead to the creation of more reactive sites, increasing the likelihood of defect formation and influencing the overall performance of the QDs.[28] The implementation of ligand-driven facet control enables significant improvement in emission efficiency for larger heavy-metal-free InAs-based QDs, particularly in the infrared range, by effectively minimizing interfacial defects. For the uniform growth of larger InAs, the continuous injection method was employed as it offers precise control over monomer concentration compared to the hot injection method, enabling the enhanced size control while maintaining excellent particle size uniformity. Furthermore, we introduce a one-pot synthesis method for InAs/InZnP/ZnSe/ZnS core/multi-shell growth, which significantly improves PLQY in both the NIR and SWIR regions. Our systematic investigation reveals that the choice of ligand not only influences the morphology of QDs but also fundamentally affects their optical properties.[29–33] Furthermore, the exciton dynamics of InAs-based QDs in the infrared region are investigated using transient absorption spectroscopy (TA) with an ultrafast femtosecond laser. This technique demonstrates how reduced interfacial defects through facet control contribute to the observed improvements in PLQY.

The novelty of this research lies in our direct manipulation of facet exposure through ligand adsorption, enabling precise control over QD morphology and defect formation. In addition, a one-pot synthesis method for core–shell passivation further extends these improvements of PLQY across both NIR and SWIR regions. This research not only contributes to a deeper understanding of exciton dynamics in infrared-emitting QDs but also sets the foundation for developing high-efficiency, heavy-metal-free QDs that can be scaled for a wide range of infrared applications. By successfully addressing defect reduction and achieving precise morphological control, this study presents a promising approach for overcoming the limitations of existing QD technologies, paving the way for future advancements in infrared optoelectronics.

Results and discussion

Synthesis and ligand-driven facet control of InAs QDs

In this study, we employed strategic ligand selection during the continuous injection process to control both the morphology and facet exposure of InAs QDs throughout their size evolution. By optimizing initial reaction volume, injection rate, and reaction temperature parameters, we successfully synthesized uniform-size InAs QD cores spanning emission wavelengths from NIR to SWIR regions (Fig. S1†). However, achieving uniform QD growth for SWIR emission beyond 1 μm wavelength presents significant challenges. As the core size increases, PLQY can be influenced by multiple factors. QDs with smaller cores tend to exhibit high PLQY regardless of shell thickness, which may be attributed not only to lower defect density but also to the stronger quantum confinement effect in smaller QDs. In contrast, larger cores may be more affected by the increase in interfacial defects and strain effects that can arise during shell formation. This relationship between core size and PLQY has also been reported in previous studies.[27] This strain at the core–shell interface causes interfacial defects, explaining why achieving high PLQY for long-wavelength emission in the infrared region using heavy-metal-free InAs-based QDs has remained challenging, as evidenced in Table S1.†[25,26] For this reason, we focused on facet control of QDs to address the critical issue of interfacial defects that become increasingly pronounced with expanding QD dimensions.

Ligand selection plays a pivotal role in controlling both the growth rate and exposed facets of QDs.[29,32] When ligands strongly adsorb onto the QDs, they not only restrict growth but also determine predominant facets based on the adsorption energies between ligands and individual facets, thereby controlling facet-specific growth rates.[28] In this study, palmitic acid served as the primary ligand for the indium precursor through complex formation with indium acetate, while dioctylamine or oleic acid functioned as ligands for the arsenic precursor, enabling controlled continuous injection of InAs nanoclusters.[34] Notably, a mixed ligand system was employed, with dioctylamine or oleic acid used alongside palmitic acid. This combination allowed for fine-tuning of both the growth rate and the exposed facets of the QDs, as ligand interactions with specific facets influenced their adsorption energies and facet-specific growth rates. As shown in Fig. 1, a distinct difference in the 1S peak was observed depending on the ligand used. With dioctylamine, a 1S peak appeared at 1270 nm after 26 hours (Fig. 1a), whereas oleic acid facilitates more rapid growth, producing a 1S peak at 1300 nm within just 12 hours (Fig. 1b). This marked difference in growth rates stems from distinct growth mechanisms induced by the respective ligands. Furthermore, Fourier-transform infrared (FTIR) spectra (Fig. S2†) confirmed successful differential ligand adsorption on each InAs core surface, validating our ligand-specific surface modification approach.

Fig. 2 shows UV-vis absorption spectra where a 1S peak at 1100 nm represents an intermediate growth stage of InAs QDs.

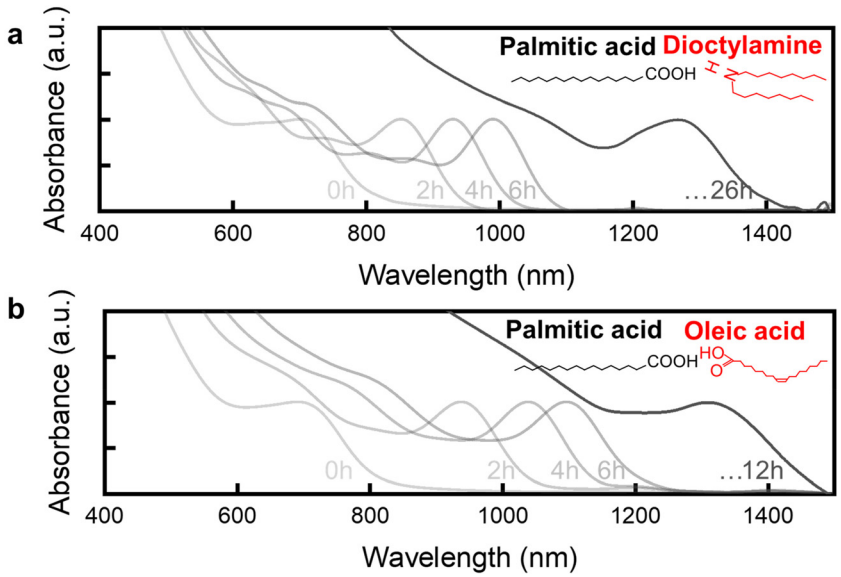

Fig. 1 Absorption spectra over time for different ligands: (a) Absorption spectra of InAs QDs with dioctylamine as a ligand, with aliquots taken between 0 and 26 hours. (b) Absorption spectra of InAs QDs with oleic acid as a ligand, with aliquots taken between 0 and 12 hours.

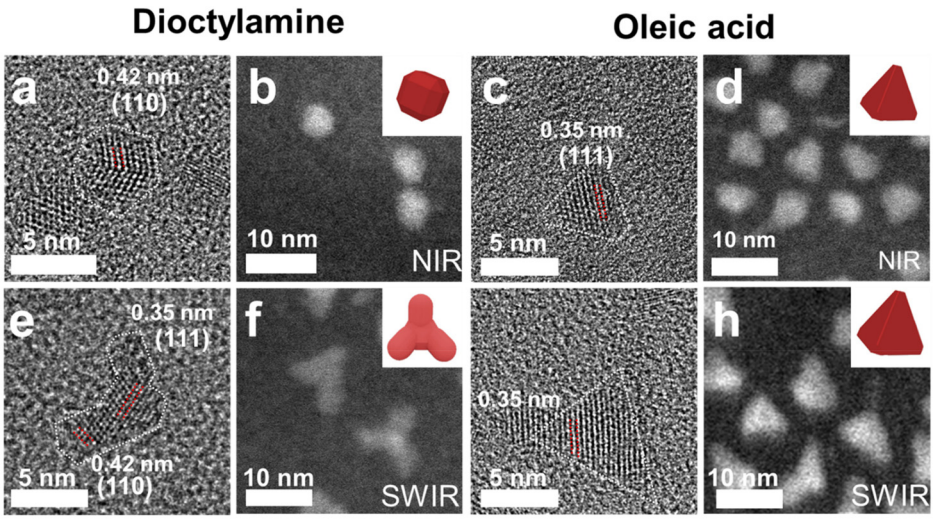

Fig. 2 HRTEM and STEM images of NIR and SWIR QDs with different ligands: (a and b) NIR QDs (1S: 1100 nm) with dioctylamine; (c and d) NIR QDs (1S: 1100 nm) with oleic acid; (e and f) SWIR QDs (1S: 1300 nm) with dioctylamine; (g and h) SWIR QDs (1S: 1300 nm) with oleic acid.

As is well known, the (110) facet is nonpolar, whereas the (111) facet is polar (see Table S2† for details). QDs synthesized with dioctylamine displayed a hybrid facet composition, combining both (110) and (111) facets, resulting in predominantly spherical morphology (Fig. 2a and b). In contrast, QDs grown with oleic acid preferentially formed polar (111) facets, adopting a distinctive tetrahedral morphology (Fig. 2c and d). These morphological differences became increasingly pronounced as QD size increased into the SWIR region. For QDs exhibiting a 1S peak at 1300 nm in the SWIR region, dioctylamine-mediated synthesis produced tetrapod shape, characterized by arms extending along the (111) facet direction while keeping nonpolar (110) facets exposed along their width (Fig. 2e and f). Conversely, oleic acid-mediated growth resulted in more pronounced tetrahedral shape with predominantly exposed polar (111) facets (Fig. 2g and h). These structural and morphological differences in InAs QDs, depending on the ligand used, are further supported by X-ray diffraction (XRD) patterns (Fig. S3†) and fast fourier transform (FFT) analysis (Fig. S4†).

The morphology and growth of InAs QDs varied significantly depending on the type of ligand used (Fig. S5†). Carboxylic acid ligands, such as only palmitic acid, which has weak adsorption, produced tetrapod structures when used alone.[35] However, combining palmitic acid and oleic acid in a

2 : 1 ratio resulted in tetrahedron-shaped QDs. Amine ligands exhibited distinct growth characteristics based on their binding strength (oleylamine > dioctylamine > trioctylamine):[36] oleylamine led to slow growth and spherical QDs, dioctylamine facilitated fast and uniform tetrapod growth, and trioctylamine, due to its weak binding, caused the formation of amorphous QDs. Even in cases where amine is only partially present, the core claim of this study—that the presence of mixed ligands leads to the predominant exposure of different surfaces—remains valid, as the influence of the ligands on surface characteristics persists. These findings emphasize the pivotal role of ligand selection in controlling the growth and morphology of InAs QDs.

Growth mechanisms and facet exposure

This study comprehensively demonstrates that ligand selection exerts decisive influence not only on facet exposure but also on the overall growth mechanism of InAs QDs. Specifically, the interaction between ligands and precursors significantly modulate reaction kinetics, which, in turn determines both morphological development and facet distribution of the QDs. To establish a comprehensive understanding of the mechanistic principles governing QD formation, we conducted two complementary analyses: first, we performed density functional theory (DFT) calculations to quantify surface energetics of different facets, and second, we investigated the detailed reaction pathways to elucidate how different ligands influence the growth kinetics. Through this dual analytical approach, we aimed to bridge the gap between theoretical predictions and experimental observations in QD synthesis.

Fig. 3a and b presents DFT calculations of surface stabilization energies for dioctylamine and oleic acid interactions with the (110) and (111) facets of InAs QDs. For computational efficiency, dioctylamine was modeled as diethylamine and oleic acid as propionic acid in these DFT calculations. Amine ligands provide similar stabilization effects on both facets (−0.54 and −0.70 eV for (110) and (111) facets, respectively). However, considering the bare (110) facet is inherently more

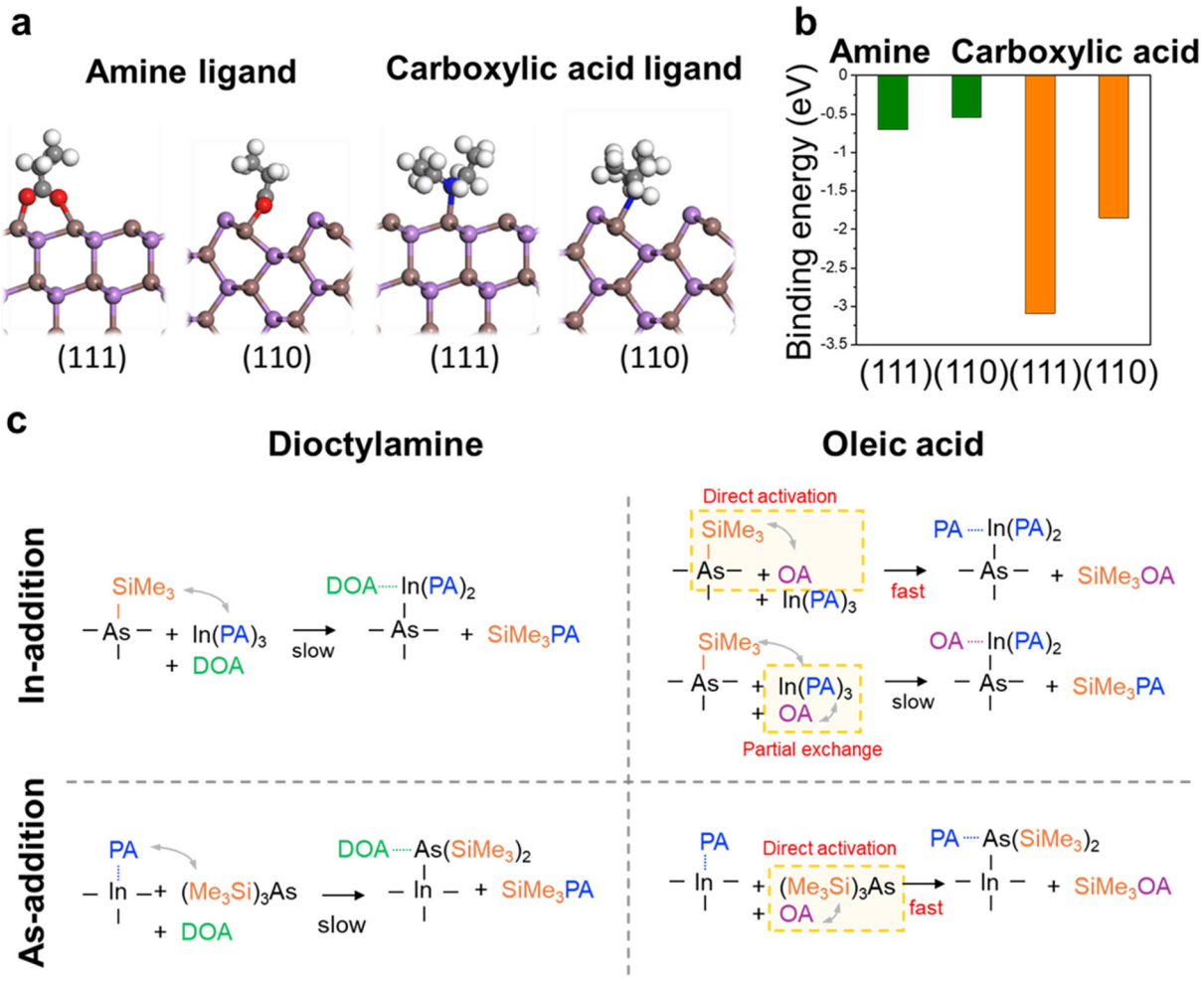

Fig. 3 (a) Optimized DFT structures showing amine and carboxylic acid ligand binding configurations on InAs (111) and (110) facets. (b) Calculated binding energies of amine and carboxylic acid ligands on different crystal facets. (c) Reaction mechanisms of InAs QDs formation through In-addition and As-addition pathways depending on the ligands. DOA, OA and PA present dioctylamine, oleic acid, and palmitic acid, respectively.

stable (Table S2†), thereby dioctylamine-mediated growth primarily proceeds on the (110) facet. The small energy difference between (110) and (111) surfaces resulting from amine binding can induce asymmetric arm development in tetrapods, predominantly exposing the stable (110) surface. In contrast, oleic acid generates a substantial difference in surface stabilization between facets, with DFT calculations indicating that carboxylic acid provides over 1.2 eV greater stabilization to the (111) facet compared to the (110) facet facets (−3.09 eV and −1.85 for (111) and (110) facets, respectively), as shown in Fig. 3a. This enhanced stabilization leads to (111) facet predominance in QDs, resulting in tetrahedral morphology. Considering the indium site density of approximately 1 atom per 15 $Å^2$ on the cluster surface, a ligand that provides at least 0.6 eV of additional binding energy – calculated as the difference in surface energy divided by the indium site density – promotes the formation of (111) facet. This requirement is satisfied by oleic acid. These DFT results are consistent with experimental observations, where dioctylamine produces QDs with dominant (110) facets, while oleic acid yields QDs with a predominant (111) facets.

Based on these DFT findings, we conducted a detailed analysis of the distinct reaction pathways and kinetics associated with dioctylamine and oleic acid. Fig. 3c illustrates how the indium precursor, arsenic precursor, and the respective ligands – dioctylamine and oleic acid – influence the mechanistic pathways in InAs QD synthesis.[34] In the [In-addition] step, $In(PA)_3$ directly reacts with $-As(SiMe_3)_n$ on the cluster surface to form In–As bonds while generating $SiMe_3PA$ through Lewis acid–base coupling.[34] In the presence of dioctylamine, this reaction proceeds slowly, primarily governed by the slow formation rate of $SiMe_3PA$. This slower reaction rate can be attributed to the interaction between bulky precursors and the ligand-stabilized cluster surface, where dioctylamine primarily provides a surface stabilization effect rather than directly participating in the reaction. In contrast, oleic acid demonstrates a dual-mechanism for enhancing the reaction. It exhibits the capability to directly activate $-As(SiMe_3)_n$, thereby facilitating more efficient In–As bond formation compared to amine ligands. In addition, oleic acid can undergo partial ligand exchange with $In(PA)_3$, increasing the reactivity of the indium precursor and providing an indirect pathway to accelerate the reaction. Similarly, in the [As-addition] process, the influence of different ligands on reaction pathways and kinetics becomes evident. With dioctylamine, the reaction proceeds slowly as $As(SiMe_3)_3$ couples with the PA ligand on the indium atom of the cluster to form In–As bonds and promote cluster growth, while dioctylamine maintains its role as a stabilizing agent. However, when oleic acid is used, the reaction demonstrates significantly enhanced kinetics due to direct activation, where oleic acid readily pairs with $As(SiMe_3)_3$ precursor, activating the arsenic species in solution phase and enhancing its reactivity. The key distinction lies in ability of oleic acid to promote more rapid and efficient InAs QD formation through direct activation of arsenic species both in QDs and solution, whereas dioctylamine primarily serves as a stabilizer, resulting in more retarded growth kinetics.

Through these analyses, we successfully synthesized InAs cores with controlled facet expose by employing distinct ligand-mediated growth mechanisms. These mechanisms led to varying growth rates and specific facet exposures. As previously mentioned, InAs-based infrared emissive QDs typically experience a decrease in emission efficiency as their size increases. This decline is attributed to several factors, including surface oxidation, interfacial defects and lattice strain between the core and shell. The impact of interfacial defects becomes more pronounced at larger sizes, and the growth of cores with different facets introduces diverse defects. With this in mind, we developed the strategy centralizing on facet control and interfacial defects prior to shell passivation.

Core–shell structure design and passivation

The InAs/InP/ZnSe/ZnS QDs core/multi-shell structure has gained attention as a promising alternative to heavy-metal cadmium-based shells for minimizing lattice mismatch.[37–42] Shell growth optimization requires minimizing lattice strain at the core/shell interface through appropriate mid-shell selection and establishing adequate energy band offsets for effective electron–hole pair confinement using an optimized multi-shell structure. The lattice constant of In_xZn_yP can be tuned from 5.86 Å for pure InP to 5.39 Å by adjusting Zn concentration, helping reduce lattice mismatch with Zn-based shells.[39,43] Following the approach represented in Fig. 4, we developed a one-pot synthesis method for InAs/InZnP/ZnSe/ZnS core–shell QDs. Given that III–V QDs have lower chemical stability and greater susceptibility to surface oxidation compared to II–VI QDs, we implemented a continuous shell layering technique. This method maintained an inert atmosphere throughout the synthesis process to prevent oxidation. The resulting structure comprises an InAs/InZnP/ZnSe/ZnS core/multi-shell configuration with distinct ligand associations, as shown in Fig. 4b.

The process was optimized by gradually increasing InZnP content proportional to InAs nanoclusters. Successful InZnP layering on InAs was confirmed by a red shift in the 1S peak, as shown in Fig. S6.† The extent of this shift correlates with InZnP passivation quality, similar to shifts observed with ZnSe shell addition, showing minimal difference from the Zn shell.[43] Emission efficiency QDs using dioctylamine improved significantly, as detailed in Table S3.† PLQY measurements revealed insufficient InZnP deposition limited the effectiveness of subsequent ZnSe passivation. However, with proper mid-shell InZnP passivation followed by additional ZnSe and ZnS shells, PLQY increased to 40.9%. We applied this method across different core sizes to determine optimal passivation conditions (Fig. S7, S8 and S9†). The substantial lattice mismatch between InAs and ZnSe induces numerous interfacial traps when mid-shell deposition is inadequate, leading to sharp decline in PLQY, underscoring the critical role of mid-shell in minimizing interfacial defects for enhanced emission efficiency.

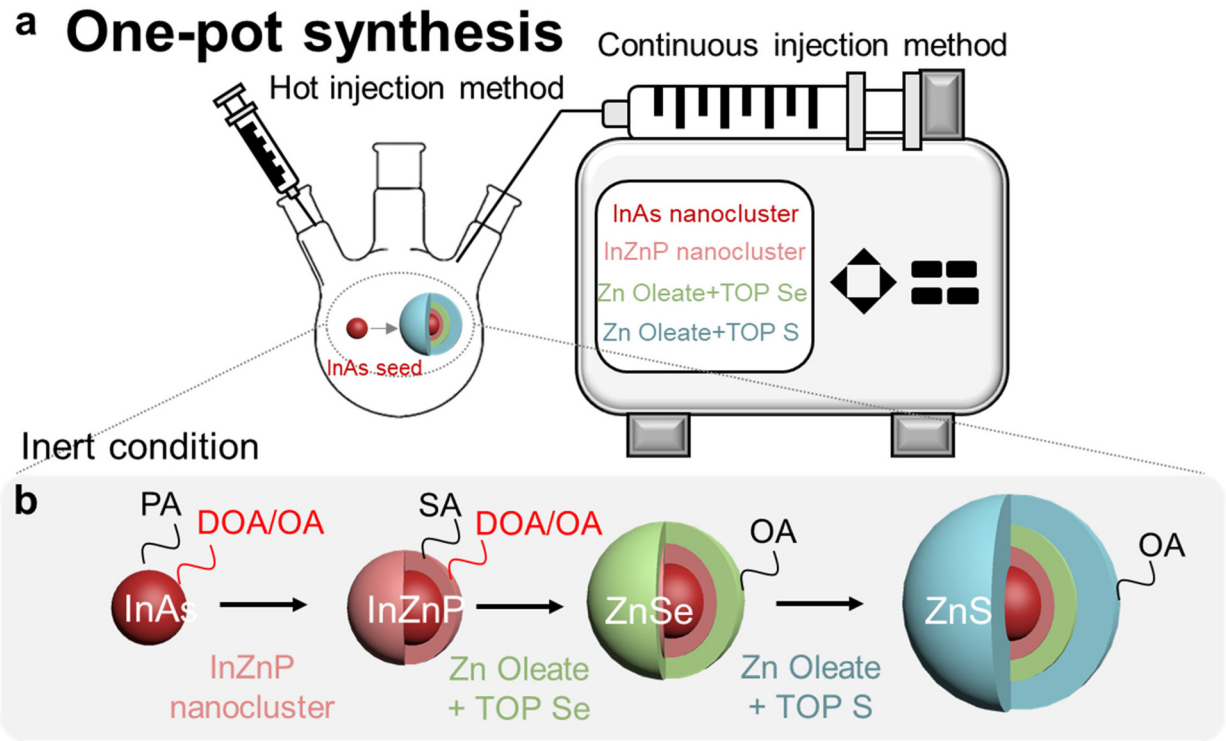

Fig. 4 (a) Schematic diagram of the one-pot synthesis of InAs seed through the hot injection method and InAs/InZnP/ZnSe/ZnS core/multi shell through the continuous injection method. (b) Structure of InAs/InZnP/ZnSe/ZnS core/multi shell with different ligands; palmitic acid (PA), stearic acid (SA), dioctylamine (DOA), oleic acid (OA), and trioctylphosphine (TOP).

To isolate the effects of facet control on core/shell interfacial defects and their impact on optical properties of InAs-based QDs, we conducted all syntheses under inert atmosphere *via* one-pot approach, minimizing exposure to oxygen and moisture that could introduce surface defects. During the synthesis, we analyzed aliquots at each stage—InAs core, InAs/InZnP, and InAs/InZnP/ZnSe passivated QDs—after air exposure. As shown in Fig. 5a, XRD analysis revealed indium oxide peaks immediately upon air exposure for InAs and InZnP samples, which disappeared after ZnSe passivation. Further X-ray photoelectron spectroscopy (XPS) measurements provided detailed analysis of oxide peak types and intensities.[9,10] As shown in Fig. 5b, the In 3d XPS spectra confirm the presence of InAs across all samples. Notably, the pronounced In_2O_3 peaks significantly diminished after ZnSe growth (InAs/In(Zn)P/ZnSe), indicating effective passivation by ZnSe. A similar trend is observed in the As 3d XPS spectra (Fig. 5c), where oxide presence was substantially reduced after ZnSe passivation. These results demonstrate that our one-pot approach, where InAs/InZnP/ZnSe core/shell/shell morphology emerges from InAs in one reaction step, effectively prevents oxidation despite the partial presence of P-related traps (Fig. S10†).

To remove these interfacial traps, we employed hydrofluoric acid (HF) treatment, as fluoride ions effectively eliminate P dangling bonds.[44–46] XPS analysis confirmed reduced phosphine oxide content after HF treatment in Fig. S10.† During the one-pot synthesis of the InZnP shell, appropriately controlled HF addition facilitated the effective removal of interfacial traps. This led to a reduction in non-radiative recombination (fast decay) and an increase in radiative recombination (slow decay), as demonstrated in Fig. S12,† with corresponding decay rates and ratios detailed in Table S4.† Consequently, the process resulted in enhanced PLQY, as shown in Table S5.† This comprehensive surface property analysis highlights the importance of shell passivation in enhancing emission efficiency of III–V QDs, while enabling us to isolate the effects of core facet control on optical properties by eliminating other influencing factors.[47]

Facet-dependent interfacial defects and optical properties

After mitigating oxidation effects, we explored how facet-dependent interfacial defects influence QD emission efficiency across NIR and SWIR regions.[48] The NIR region spans wavelengths from 0.75 to 1.4 μm, while the SWIR region extends from 1.4 to 3 μm. This study introduces a novel method to eliminating core/shell interfacial defects in QDs emitting up to the SWIR range, with a specific focus on addressing facet-dependent interfacial defects. Dioctylamine-mediated growth exposes nonpolar (110) facets, which are more stable and maintain stoichiometric surfaces, resulting in fewer interfacial traps. In contrast, oleic acid promotes polar (111) facets, leading to the formation of cation-rich dangling bonds and increased interfacial traps (Fig. S13†).[37,49,50]

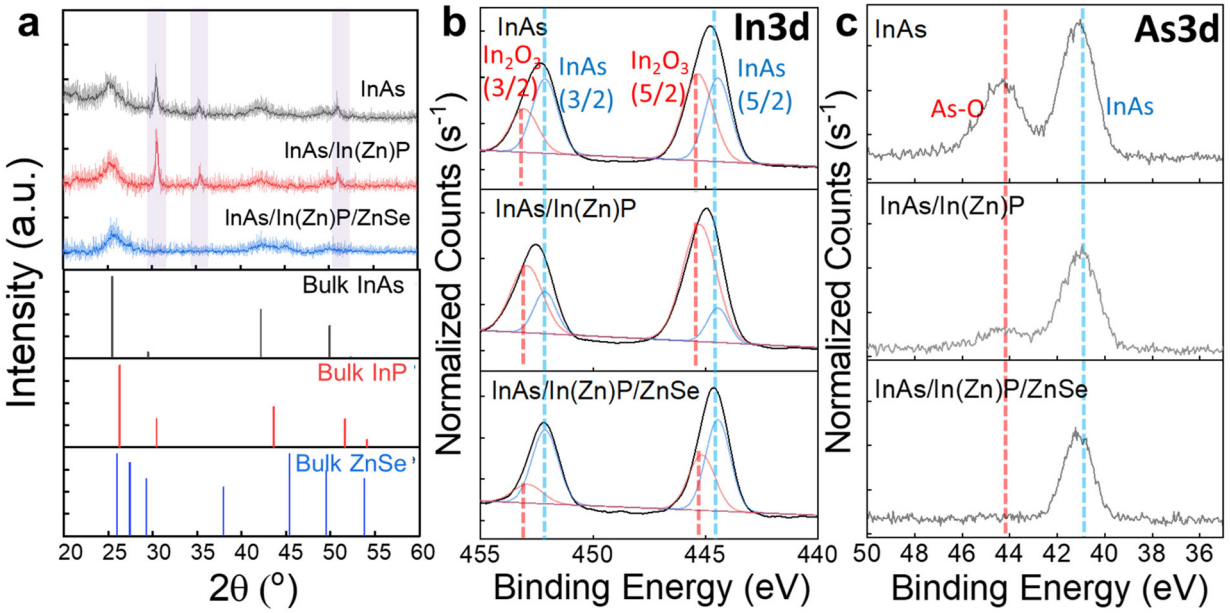

Fig. 5 (a) The X-ray diffraction (XRD) patterns of InAs, InAs/InZnP, and InAs/InZnP/ZnSe core/shell QDs using dioctylamine as a ligand. (b–d) X-ray photoelectron spectroscopy (XPS) spectra showing the elemental composition of InAs-based QDs. XPS spectrum for (b) In 3d, (c) As 3d of InAs, InAs/InZnP, and InAs/InZnP/ZnSe QDs.

As shown in Fig. 6, we analyzed the optical properties of HF-treated InAs/InZnP/ZnSe/ZnS core/multi-shell QDs being grown for NIR and SWIR emission. Comparing optical properties of QDs synthesized with different ligands (dioctylamine *vs.* oleic acid), we focused on NIR emission around 1250 nm and SWIR emission above 1400 nm. PLQY measurements showed consistently higher values for dioctylamine-mediated QDs compared oleic acid-mediated QDs at equivalent wavelengths. Specifically, at λ_{PL} = 1260 nm, dioctylamine-mediated QDs achieved 39% PLQY (Fig. 6a), surpassing the 29% PLQY of oleic acid-mediated QDs (Fig. 6b). At λ_{PL} = 1420 nm, while both types showed decreased PLQY, dioctylamine-mediated QDs maintained 7.3% (Fig. 6c), retaining 18.7% of their initial value, whereas oleic acid-mediated QDs dropped more significantly to 2.6% (Fig. 6d), preserving only 9% of their initial PLQY. Although increasing QD size led to PLQY reduction due to core–shell lattice strain and interfacial defects,[25,26] the reduction was notably less severe in dioctylamine-mediated QDs compared to oleic acid-mediated QDs, particularly in the SWIR region above 1400 nm. These results represent excellent efficiency for heavy metal-free QDs in infrared emission wavelengths (NIR: 750–1400 nm and SWIR: 1400–3000 nm), as summarized in Table S1.† While QD size increases typically lead to performance degradation due to interfacial defects,[25,26] our facet control approach effectively mitigates these defects and enhances emission efficiency. This ligand-mediated facet control strategy improves emission efficiency even at longer infrared wavelengths, while also maintaining consistent dispersibility and stable emission properties over time regardless of the ligand used. Furthermore, achieving high emission efficiency without heavy metals underscores this approach's significance in developing environmentally friendly, high-efficiency infrared emissive nanomaterials. Furthermore, achieving high emission efficiency without heavy metals underscores the significance of this approach in developing environmentally friendly, high-efficiency infrared emissive nanomaterials.

To understand the relationship between ligand effect QD morphology, interfacial defects, and PLQY variations, we investigated the underlying exciton dynamics using transient absorption (TA) spectroscopy.[21,51–53] Femtosecond pump–probe TA spectroscopy measures rapid dynamic changes following ultrafast laser pulse absorption by QDs, enabling analysis of charge carrier behavior. This technique provides important information about charge transfer, recombination, and energy transfer within QDs. In InAs QDs, the band edge exhibits two-fold degeneracy, though the hole states at this edge are considered dark.[54] Therefore, TA spectroscopy can be employed to study the behavior of electrons, which are optically active.[54]

It is known that the magnitude of normalized transient bleach signal by absorption ($-\Delta A/A$) in ground state bleaching (GSB) increases near the band edge energy excitation, indicating reduced charge loss or higher carrier density at the band edge;[51,52] at higher energy excitations, charge trapping becomes a significant factor. We devised a method of separately exciting the core and shell of the QDs to analyze interfacial defects. The QDs were excited with an average exciton number of approximately 0.1 per dot. The exciton number was calculated by considering the different absorption cross-sections at each wavelength, which are proportional to the absorption. When the core is excited at 700 nm, the generated elec-

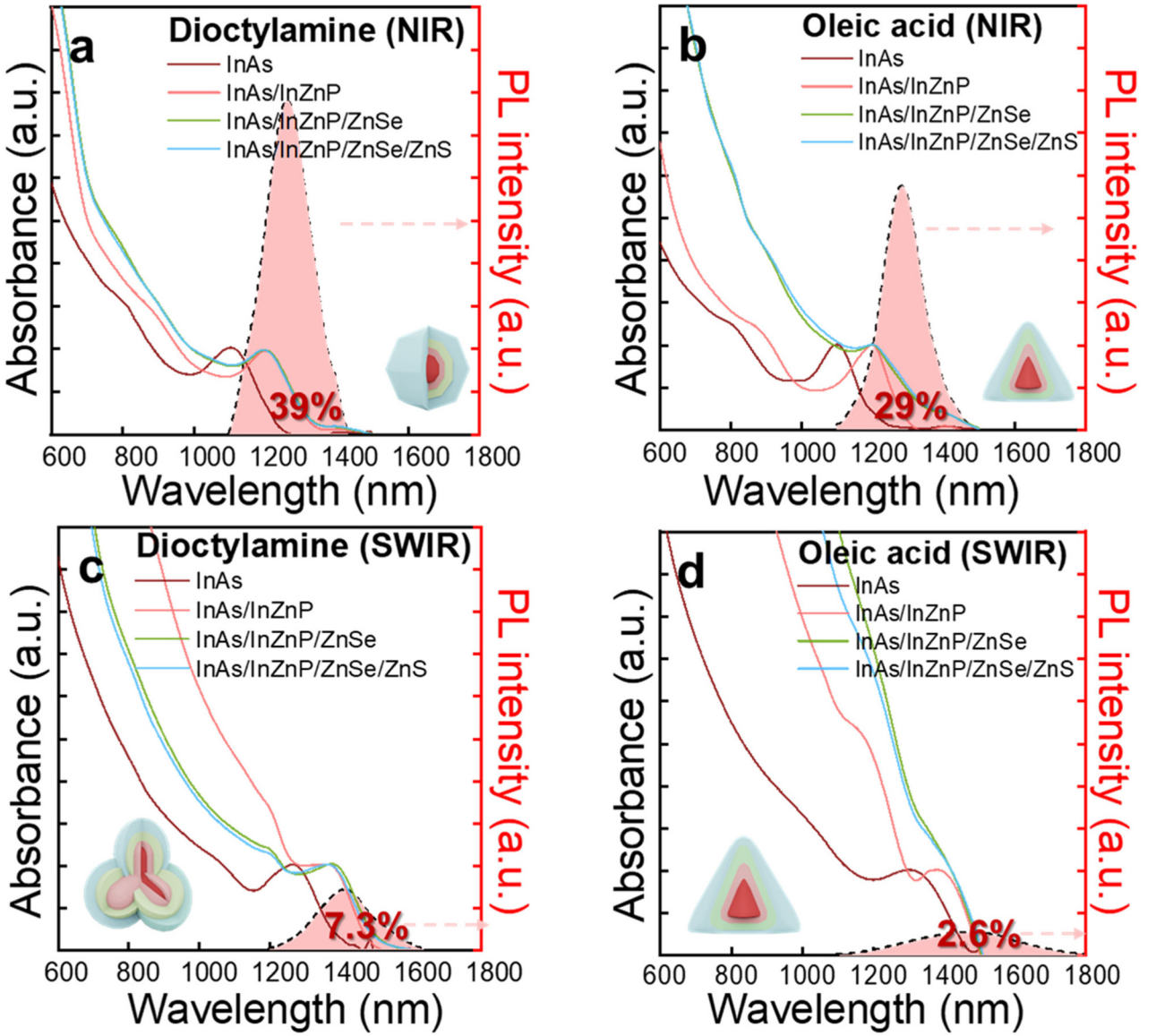

Fig. 6 Optical properties of QDs emitting at approximately 1250 nm (NIR) and above 1400 nm (SWIR) using different ligands: NIR-emitting QDs with (a) dioctylamine exhibited a PLQY of 39%, whereas (b) those with oleic acid showed a PLQY of 29%. In the SWIR region, (c) dioctylamine-based QDs achieved a PLQY of 7.3%, while (d) oleic acid-based QDs achieved a PLQY of 2.6% above 1400 nm.

trons in the core decay back at the band edge ($\langle N \rangle \sim 0.1$). In contrast, when the shell is excited separately at an excitation wavelength of 400 nm with the same exciton number, the electrons excited in the shell rapidly transfer to the core and decay together there. Consequently, the magnitude of $-\Delta A/A$ in GSB should be nearly identical at different excitation wavelengths. However, if interfacial traps are present, the electrons get trapped at interfaces, reducing $-\Delta A/A$ at the band edge and decreasing PLQY, particularly at higher energy excitation. We observed a clear relationship between interfacial defects, PLQY and $-\Delta A/A$, confirming that both $-\Delta A/A$ and PLQY decrease with increasing excitation energy. For example, treating the QDs with HF to eliminate interfacial traps reduced the differences in PLQY and $-\Delta A/A$ across different excitation wavelengths (Fig. S14†). Additionally, when the InAs core QDs were excited at different wavelengths, the $-\Delta A/A$ magnitude remained nearly identical decay (>5 ps) (Fig. S15†).

Fig. 7 shows the results of examining the interfacial states of core/shell structured QDs with different facets through charge behavior. The $-\Delta A/A$ at 400 nm was normalized relative to the maximum $-\Delta A/A$ value at 700 nm. For QDs using dioctylamine (39% PLQY with nonpolar facets in core) showed a small difference in $-\Delta A/A$ between 400 nm and 700 nm excitations compared to QDs using oleic acid (29% PLQY with polar facets in core), as shown in Fig. 7a and b. When using dioctylamine, $-\Delta A/A$ decreased to 17% of the initial value, whereas in the case of oleic acid, it decreased to 10%, as calculated by comparing the GSB signals at 700 nm and 400 nm

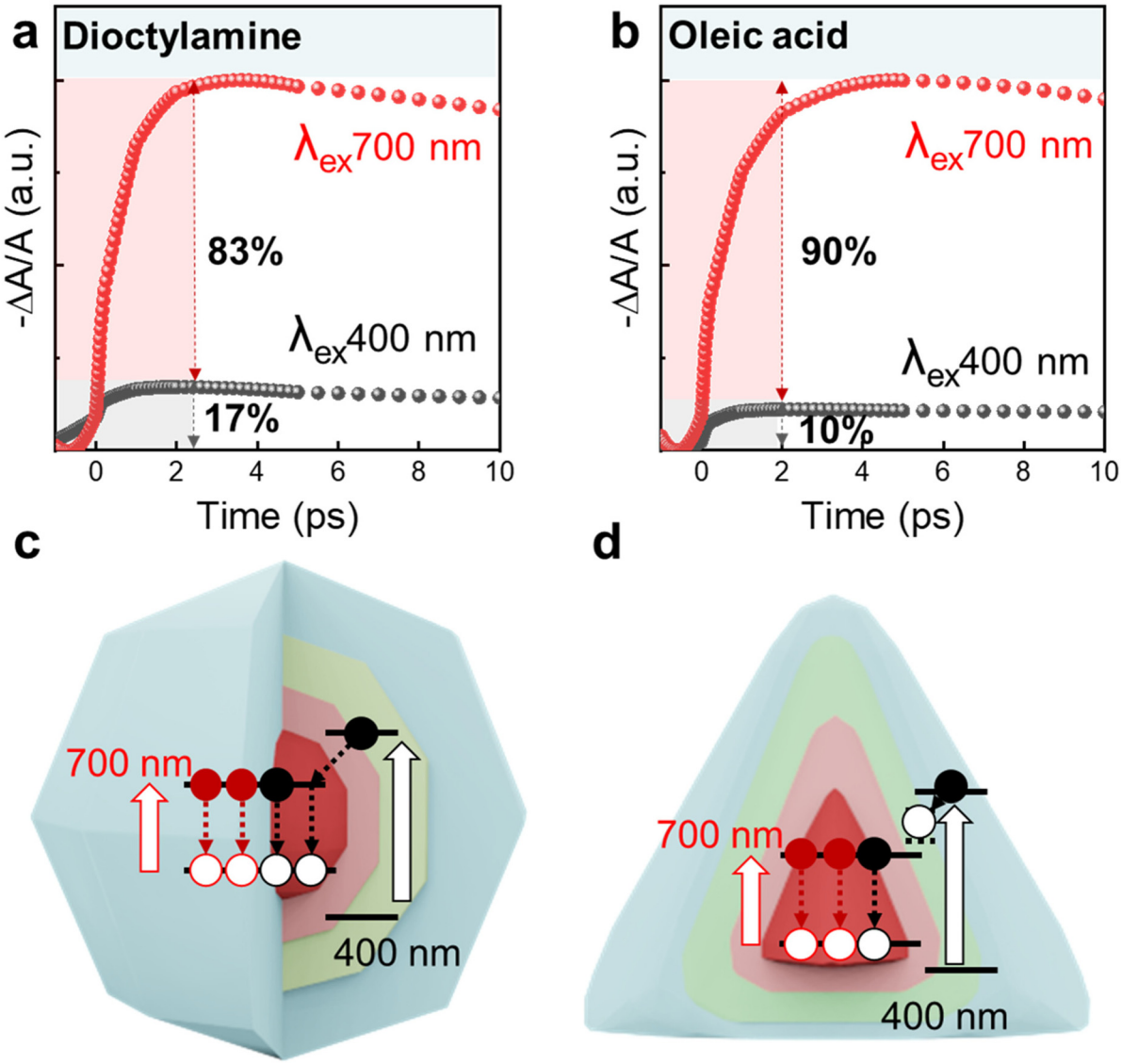

Fig. 7 Ground state bleaching (GSB) $-\Delta A/A$ at 1200 nm for QDs excited at different wavelengths (400 nm and 700 nm): (a) using dioctylamine as the ligand, (b) using oleic acid as the ligand. Schematic diagram of QDs excited at different wavelengths: (c) using dioctylamine, (d) using oleic acid as the ligand.

excitations. In addition, the TA spectroscopy results also revealed that, upon analyzing the decay rates in GSB at different wavelengths, the fast decay rate representing non-radiative recombination was found to be faster in oleic acid-mediated QDs compared to dioctylamine-mediated QDs, as shown in Table S6.† This indicates that a larger proportion of charges excited in QDs are trapped in cases where there are more interfacial traps. This confirms that the difference in $-\Delta A/A$ values observed in the core/shell structure is due to electron trapping and subsequent loss as the electrons transfer from shell to core. As a result, as shown in Fig. 7c, dioctylamine-mediated QDs exhibit more efficient electron transition from shell to core at the band edge when the shell is separately excited, compared to oleic acid-mediated QDs (Fig. 7d), resulting in enhanced optical properties. These findings highlight that the optical properties of QDs depend on core facets, with exciton dynamics analysis validating this relationship. The research underscores the importance of ligand-driven facet control in enhancing QDs emission efficiency in NIR and SWIR region.

Conclusions

In this study, we improved InAs QDs for enhanced infrared emission through strategic synthesis condition optimization. Using a continuous injection process combined with facet control through different ligands (dioctylamine and oleic acid), we achieved uniform size growth while minimizing interfacial defects. The two ligands demonstrated distinct influ-

ences on QD growth: dioctylamine promoted slower growth favoring nonpolar facets and yielding spherical or tetrapod shapes, while oleic acid induced faster growth favoring polar facets and resulting in tetrahedron shapes. Passivating InAs/InZnP/ZnSe/ZnS QDs with a one-pot synthesis minimized oxidation effect, yielding dioctylamine-based cores with 39% PLQY, compared to 29% for oleic acid-based cores. This performance advantage extended into the SWIR region above 1400 nm, where dioctylamine-based QDs achieved 7.3% PLQY, an excellent value for heavy metal-free QDs, compared to 2.6% for oleic acid-based QDs. TA spectroscopy confirmed that dioctylamine-based QDs exhibited higher PLQY and smaller GSB variations across different excitation wavelengths compared to oleic acid-based QDs. The reduced GSB decay difference between core-only and shell excitation in dioctylamine-based QDs indicated fewer interfacial traps, while oleic acid-based QDs showed larger differences, suggesting increased interfacial charge carrier trapping at the interface and reduced overall emission efficiency. These findings underscore the crucial role of ligand-driven facet control in enhancing QD emission efficiency across both NIR and SWIR regions, advancing capabilities beyond conventional QD applications.

Experimental section

Methods

Materials and chemicals. Indium acetate (99.99%, Sigma Aldrich), tetrachloroethylene (TCE, anhydrous, ≥99%, Sigma Aldrich), trioctylphosphine (TOP, 97%, Sigma Aldrich), dioctylamine (97%, Sigma Aldrich), palmitic acid (≥99%, Sigma Aldrich), stearic acid (95%, Sigma Aldrich), 1-octadecene (90%, Sigma Aldrich), oleic acid (90%, Sigma Aldrich), tris(trimethylsilyl)amine ($TMSi_3As$, JSI Silicon), tris(trimethylsilyl)phosphine ($TMSi_3P$, 20% in TOP, Uniam), zinc acetate dihydrate (98%, Sigma Aldrich), trioctylamine (98%, Sigma Aldrich), selenium (powder, 99.99%, Sigma Aldrich).

Synthesis of InAs/InZnP/ZnSe/ZnS QDs

InAs seed. In a three necks flask, indium acetate (0.145 g), palmitic acid (0.384 g), and octadecene (2.5 mL) were combined and degassed under vacuum at 110 °C for 2 hours to remove dissolved gases and moisture. The system was then switched to an inert atmosphere and heated to 300 °C. Separately, a solution was prepared inside a glove box by mixing $TMSi_3As$ (0.07 g), dioctyl amine or oleic acid (0.18 g or 0.24 mL), and octadecene (0.5 mL). This solution was swiftly injected into the reaction vessel at 300 °C.

InAs nanocluster. In a three-neck flask, indium acetate (1.45 g), palmitic acid (3.84 g), and octadecene (25 mL) were combined and degassed under vacuum at 110 °C for 2 hours to remove dissolved gases and moisture. The system was then switched to an inert atmosphere and cooled to 25 °C. Separately, a solution was prepared inside a glove box by mixing $TMSi_3As$ (0.7 g), dioctyl amine or oleic acid (1.8 g or 2.4 mL), and octadecene (5 mL). This solution was slowly injected into the reaction flask at room temperature.

InZnP nanocluster. In a suitable reaction vessel, indium acetate (0.87 g), zinc acetate (0.2751 g), stearic acid (3.39 g), and octadecene (20.1 mL) were combined and degassed under vacuum at 110 °C for 2 hours to remove dissolved gases and moisture. The system was then switched to an inert atmosphere and allowed to cool to room temperature. Separately, a solution was prepared inside a glove box by mixing 6 mL of $TMSi_3P$ (10 wt% in TOP), dioctyl amine (1.44 g), and octadecene (3.99 mL). This solution was slowly injected into the reaction vessel at room temperature.

Subsequently, the InAs seeds were used to form InAs QDs. The reaction mixture was heated to 300 °C under an inert atmosphere, and the previously prepared InAs nanocluster solution was injected into the reaction vessel containing the InAs seed solution at a rate of 1 mL h^{-1} until the target wavelength was achieved. Subsequently, InZnP nanocluster solution was injected in the same way, optimized for each size: 20 mL for NIR QDs and 25 mL for SWIR QDs. After the injection of InZnP nanocluster, the temperature was reduced from 300 °C to 150 °C. Then, 600 μL of 1 M HF dispersed in acetone was added to the reaction mixture and left for 10 minutes. Afterward, the temperature was raised back to 300 °C. Following this, a 4 mL of 0.5 M zinc–oleate solution was injected into the mixture, immediately followed by the injection of TOP-Se, 3.0 mL for NIR and 3.5 mL for SWIR, at a rate of 3.0–3.5 mL h^{-1}.

Density functional theory calculation. Density functional theory (DFT) calculations were performed using the Vienna *Ab initio* Simulation Package (VASP).[55] The Perdew–Burke–Ernzerhof (PBE) functional was employed for the exchange–correlation potential within the generalized gradient approximation (GGA). The projector augmented wave (PAW) method was used to describe the electron-ion interactions. A plane-wave basis set with a kinetic energy cutoff of 400 eV was utilized. The Brillouin zone was sampled using a Monkhorst–Pack *k*-point mesh of 3 × 3 × 1 for surface calculations. Geometry optimizations were performed until the forces on all atoms were less than 0.02 eV $Å^{-1}$. A vacuum layer of at least 15 Å was included in the surface slab models to prevent interactions between periodic images. Binding energies were calculated differently for amine and carboxylic acid ligands. For amines, the reference state was the infinitely separated amine molecule from the surface. For carboxylic acids, to obtain the binding energy of the ionic state, we placed the carboxylic group's proton on the opposite side of the surface and calculated the energy required to remove the carboxylate anion to the vacuum region.

Characterization

Surface characterization. The XRD measurements were performed using an Ultima IV diffractometer (Rigaku, Japan). The XPS measurements were performed using a Nexsa G2 spectrometer (Thermo Scientific, USA). FTIR spectroscopy measurements were conducted using a Bruker Alpha spectrometer to analyze the surface ligands of the QDs.

Morphology characterization. The TEM measurements were performed using a Talos F200X G2 microscope (Thermo Fisher, USA) for HR-TEM, STEM, FFT.

Optical characterization. The optical properties of the synthesized nanoparticles were evaluated using a UV/Vis spectrometer with an integrating sphere (UV3600, Shimadzu). We measured the photoluminescence (PL) and photoluminescence quantum yield (PLQY) in the infrared region using a Horiba Fliorolog-QM fluorescence spectrometer. Samples were prepared and placed in the spectrometer's sample holder. Light was used to excite the samples with 950 nm wavelength, and the resulting PL was detected and converted into spectra for analysis. To measure the PLQY, an integrating sphere was used to determine the absolute quantum yield. The collected data were then analyzed to calculate the PLQY.

Transient absorption spectroscopy. TA measurements were conducted using a pulsed Yb laser system (Pharos, Light Conversion) with regenerative amplification. This laser system emitted pulses at a wavelength of 1030 nm, with a pulse duration of 196 fs, and operated at a repetition rate of 200 kHz. The primary laser beam was utilized as the seed for an optical parametric amplifier (Orpheus, Light Conversion), which generated the pump beam through a second harmonic generation module. The resulting pump beam had a wavelength of 400 nm and 700 nm and a beam radius of approximately 300 μm. Part of the original 1030 nm beam was diverted to serve as the probe beam. This probe beam was passed through a delay line and focused onto a sapphire plate to create a white-light continuum using a TA spectrometer (Harpia, Light Conversion). The probe beam, with a beam radius of 105 μm, was then focused on the sample to overlap with the pump beam area. The transmitted probe beam was subsequently collected by a detector (Kymera 193i, Andor).

Author contributions

HC: investigation, conceptualization, methodology, data curation, formal analysis, writing – original draft. YK: visualization, writing – review & editing. WDK: methodology, writing – review & editing. YSP: methodology, writing – review & editing. JYW: supervision, writing – review & editing. HKL: supervision, software, methodology, writing – review & editing. DCL: supervision, project administration, writing – original draft, writing – review & editing. All authors have critically reviewed the manuscript for intellectual content, provided final approval for publication, and agreed to be accountable for all aspects of the work to ensure its accuracy and integrity.

Data availability

The data supporting this article have been included as part of the ESI.†

Conflicts of interest

There are no conflicts to declare.

Acknowledgements

This work has been supported by the National Research Foundation of Korea (NRF) under Project Numbers RS-2024-00350615, NRF-2021M3H4A3A01062960, and 2022R1A5A1033719 and the Korea Planning & Evaluation Institute of Industrial Technology (KEIT) under Project Number 20019417, and RS-2024-00440884.

References

1 C. Dabard, J. Planelles, H. Po, E. Izquierdo, L. Makke, C. Gréboval, N. Moghaddam, A. Khalili, T. H. Dang, A. Chu, S. Pierini, C. Abadie, M. Cavallo, E. Bossavit, X. Z. Xu, P. Hollander, M. Silly, E. Lhuillier, J. I. Climente and S. Ithurria, Optimized Cation Exchange for Mercury Chalcogenide 2D Nanoplatelets and Its Application for Alloys, *Chem. Mater.*, 2021, **33**, 9252–9261.

2 T. Galle, M. Samadi Khoshkhoo, B. Martin-Garcia, C. Meerbach, V. Sayevich, A. Koitzsch, V. Lesnyak and A. Eychmüller, Colloidal PbSe Nanoplatelets of Varied Thickness with Tunable Optical Properties, *Chem. Mater.*, 2019, **31**, 3803–3811.

3 L. Gao, L. N. Quan, F. P. García de Arquer, Y. Zhao, R. Munir, A. Proppe, R. Quintero-Bermudez, C. Zou, Z. Yang, M. I. Saidaminov, O. Voznyy, S. Kinge, Z. Lu, S. O. Kelley, A. Amassian, J. Tang and E. H. Sargent, Efficient near-infrared light-emitting diodes based on quantum dots in layered perovskite, *Nat. Photonics*, 2020, **14**, 227–233.

4 H. Lu, G. M. Carroll, N. R. Neale and M. C. Beard, Infrared Quantum Dots: Progress, Challenges, and Opportunities, *ACS Nano*, 2019, **13**, 939–953.

5 S. Pradhan, F. Di Stasio, Y. Bi, S. Gupta, S. Christodoulou, A. Stavrinadis and G. Konstantatos, High-efficiency colloidal quantum dot infrared light-emitting diodes via engineering at the supra-nanocrystalline level, *Nat. Nanotechnol.*, 2019, **14**, 72–79.

6 J. Qu, P. Rastogi, C. Greboval, D. Lagarde, A. Chu, C. Dabard, A. Khalili, H. Cruguel, C. Robert, X. Z. Xu, S. Ithurria, M. G. Silly, S. Ferre, X. Marie and E. Lhuillier, Electroluminescence from HgTe Nanocrystals and Its Use for Active Imaging, *Nano Lett.*, 2020, **20**, 6185–6190.

7 M.-J. Si, D. Kim, S. Jeong, M. Yang, J. Kim, S.-Y. Lee, I.-S. Lee, J. Jeong, B.-C. Kim, T. Han, B. Kim, Y. Ahn, S. Jee, Y. Jung and S.-W. Baek, Colloidal Quantum Dot Solid-Based Infrared Optoelectronics Enabled by Solution-Phase Ligand Exchange, *Korean J. Chem. Eng.*, 2024, **41**, 1–12.

8 M. Vasilopoulou, A. Fakharuddin, F. P. García de Arquer, D. G. Georgiadou, H. Kim, A. R. B. Mohd Yusoff, F. Gao, M. K. Nazeeruddin, H. J. Bolink and E. H. Sargent, Advances in solution-processed near-infrared light-emitting diodes, *Nat. Photonics*, 2021, **15**, 656–669.

9 C. Wang, J. Lin, X. Zhang, H. Dong, M. Wen, S. Zhao, S. Yuan, D. Zhu, F. Wu and Z. Mu, Efficient ultra-broad-

band NIR-II emission achieved by multi-site occupancy in $Mg_3Ga_2GeO_8$: Ni^{2+} phosphor, *J. Alloys Compd.*, 2023, **942**, 168893.

10 Y. Zhuo, F. Wu, Y. Niu, Y. Wang, Q. Zhang, Y. Teng, H. Dong and Z. Mu, Super Broadband Emission Across NIR–I and NIR–II Under Blue Light Excitation of Cr^{3+}, Ni^{2+} Co-Doped Sr_2GaTaO_6 Phosphor Achieved by Two–Site Occupation and Effective Energy Transfer, *Laser Photonics Rev.*, 2024, **18**(8), 2400105.

11 W. K. Bae and J. Lim, Nanostructured colloidal quantum dots for efficient electroluminescence devices, *Korean J. Chem. Eng.*, 2019, **36**, 173–185.

12 Y. Kim, J. Yang and M. K. Choi, Recent Advances in Transfer Printing of Colloidal Quantum Dots for High-Resolution Full Color Displays, *Korean J. Chem. Eng.*, 2024, **41**, 3469–3482.

13 H. Lee, H. Jeong, W. Jeong, Y. J. Hwang, B. An, Y. Lee, G. Kim and D.-H. Ha, Wet Chemistry Methods for Synthesizing High-Entropy Nanoparticles: A Review of the Synthesis Strategies and Various Applications, *Korean J. Chem. Eng.*, 2024, **41**, 3371–3393.

14 Y. Sung, J. Chang, S. Choi and S. Jeong, Synthesis Strategies and Applications of Non-toxic Quantum Dots, *Korean J. Chem. Eng.*, 2024, **41**, 1–27.

15 N. Taghipour, I. Tanriover, M. Dalmases, G. L. Whitworth, C. Graham, A. Saha, O. Özdemir, B. Kundu, V. Pruneri, K. Aydin and G. Konstantatos, Ultra–Thin Infrared Optical Gain Medium and Optically–Pumped Stimulated Emission in PbS Colloidal Quantum Dot LEDs, *Adv. Funct. Mater.*, 2022, **32**, 2200832.

16 N. Taghipour, G. L. Whitworth, A. Othonos, M. Dalmases, S. Pradhan, Y. Wang, G. Kumar and G. Konstantatos, Low-Threshold, Highly Stable Colloidal Quantum Dot Short-Wave Infrared Laser enabled by Suppression of Trap-Assisted Auger Recombination, *Adv. Mater.*, 2022, **34**, e2107532.

17 G. L. Whitworth, M. Dalmases, N. Taghipour and G. Konstantatos, Solution-processed PbS quantum dot infrared laser with room-temperature tuneable emission in the optical telecommunications window, *Nat. Photonics*, 2021, **15**, 738–742.

18 H. Bahmani Jalali, L. De Trizio, L. Manna and F. Di Stasio, Indium arsenide quantum dots: an alternative to lead-based infrared emitting nanomaterials, *Chem. Soc. Rev.*, 2022, **51**, 9861–9881.

19 M. Ginterseder, D. Franke, C. F. Perkinson, L. Wang, E. C. Hansen and M. G. Bawendi, Scalable Synthesis of InAs Quantum Dots Mediated through Indium Redox Chemistry, *J. Am. Chem. Soc.*, 2020, **142**, 4088–4092.

20 T. Kim, S. Park and S. Jeong, Diffusion dynamics controlled colloidal synthesis of highly monodisperse InAs nanocrystals, *Nat. Commun.*, 2021, **12**, 3013.

21 L. K. Sagar, G. Bappi, A. Johnston, B. Chen, P. Todorović, L. Levina, M. I. Saidaminov, F. P. García de Arquer, D.-H. Nam, M.-J. Choi, S. Hoogland, O. Voznyy and E. H. Sargent, Suppression of Auger Recombination by Gradient Alloying in InAs/CdSe/CdS QDs, *Chem. Mater.*, 2020, **32**, 7703–7709.

22 X. Shan, Y. Zhou, B. Li, Z. Zeng and B. Ji, Wurtzite InAs Nanocrystals with Short-Wavelength Infrared Emission Synthesized through the Cation Exchange of Cu_3As Nanocrystals, *Chem. Mater.*, 2023, **35**, 2569–2578.

23 J. H. Song, H. Choi, H. T. Pham and S. Jeong, Energy level tuned indium arsenide colloidal quantum dot films for efficient photovoltaics, *Nat. Commun.*, 2018, **9**, 4267.

24 X. Zhao, L. J. Lim, S. S. Ang and Z. K. Tan, Efficient Short-Wave Infrared Light-Emitting Diodes Based on Heavy-Metal-Free Quantum Dots, *Adv. Mater.*, 2022, **34**, e2206409.

25 K. Gong and D. F. Kelley, Lattice Strain Limit for Uniform Shell Deposition in Zincblende CdSe/CdS Quantum Dots, *J. Phys. Chem. Lett.*, 2015, **6**, 1559–1562.

26 Z. Long, G. Yang, R. Shao, Z. Chen, Y. Liu, R. Liu and H. Zhong, The Strain Effects and Interfacial Defects of Large ZnSe/ZnS Core/Shell Nanocrystals, *Small*, 2023, **20**, 2306602.

27 M. Rafipoor, D. Dupont, H. Tornatzky, M. D. Tessier, J. Maultzsch, Z. Hens and H. Lange, Strain Engineering in InP/(Zn,Cd)Se Core/Shell Quantum Dots, *Chem. Mater.*, 2018, **30**, 4393–4400.

28 H. Lee, D. E. Yoon, S. Koh, M. S. Kang, J. Lim and D. C. Lee, Ligands as a universal molecular toolkit in synthesis and assembly of semiconductor nanocrystals, *Chem. Sci.*, 2020, **11**, 2318–2329.

29 E. Cho, J. Lee, T.-G. Kim, W.-J. Son, I. Jang and D. S. Kim, Theoretical Investigation of Organic Ligands on the Surface Structure of InP Quantum Dots: Implications for Display Materials with Enhanced Surface Stability, *ACS Appl. Nano Mater.*, 2023, **6**, 21548–21555.

30 D. C. Lee, I. Robel, J. M. Pietryga and V. I. Klimov, Infrared-Active Heterostructured Nanocrystals with Ultralong Carrier Lifetimes, *J. Am. Chem. Soc.*, 2010, **132**, 9960–9962.

31 K. K. Haldar, N. Pradhan and A. Patra, Formation of hetero-epitaxy in different shapes of Au-CdSe metal-semiconductor hybrid nanostructures, *Small*, 2013, **9**, 3424–3432.

32 J. Leemans, K. C. Dumbgen, M. M. Minjauw, Q. Zhao, A. Vantomme, I. Infante, C. Detavernier and Z. Hens, Acid-Base Mediated Ligand Exchange on Near-Infrared Absorbing, Indium-Based III-V Colloidal Quantum Dots, *J. Am. Chem. Soc.*, 2021, **143**, 4290–4301.

33 C. Pak, J. Y. Woo, K. Lee, W. D. Kim, Y. Yoo and D. C. Lee, Extending the Limit of Low-Energy Photocatalysis: Dye Reduction with PbSe/CdSe/CdS Core/Shell/Shell Nanocrystals of Varying Morphologies under Infrared Irradiation, *J. Phys. Chem. C*, 2012, **116**, 25407–25414.

34 L. Angele, S. Dreyfuss, B. Dubertret and N. Mezailles, Synthesis of Monodisperse InP Quantum Dots: Use of an Acid-Free Indium Carboxylate Precursor, *Inorg. Chem.*, 2021, **60**, 2271–2278.

35 T. Morris and T. Zubkov, Steric effects of carboxylic capping ligands on the growth of the CdSe quantum dots, *Colloids Surf., A*, 2014, **443**, 439–449.

36 M. Michalska, A. Aboulaich, G. Medjahdi, R. Mahiou, S. Jurga and R. Schneider, Amine ligands control of the optical properties and the shape of thermally grown core/shell $CuInS_2$/ZnS quantum dots, *J. Alloys Compd.*, 2015, **645**, 184–192.

37 M. J. Enright, D. Jasrasaria, M. M. Hanchard, D. R. Needell, M. E. Phelan, D. Weinberg, B. E. McDowell, H.-W. Hsiao, H. Akbari, M. Kottwitz, M. M. Potter, J. Wong, J.-M. Zuo, H. A. Atwater, E. Rabani and R. G. Nuzzo, Role of Atomic Structure on Exciton Dynamics and Photoluminescence in NIR Emissive InAs/InP/ZnSe Quantum Dots, *J. Phys. Chem. C*, 2022, **126**, 7576–7587.

38 K. R. G. Lim, D. Darwan, H. Wijaya, Z. C. Lim, J. Shanmugam, T. Wang, L. J. Lim, W. H. Ang and Z. K. Tan, High Quantum Yield Water–Dispersed Near–Infrared In(Zn)As–In(Zn)P–GaP–ZnS Quantum Dots with Robust Stability for Bioimaging, *Adv. Mater. Interfaces*, 2020, **7**(22), 2000920.

39 F. Pietra, L. De Trizio, A. W. Hoekstra, N. Renaud, M. Prato, F. C. Grozema, P. J. Baesjou, R. Koole, L. Manna and A. J. Houtepen, Tuning the Lattice Parameter of InxZnyP for Highly Luminescent Lattice-Matched Core/Shell Quantum Dots, *ACS Nano*, 2016, **10**, 4754–4762.

40 H. Wijaya, D. Darwan, K. R. G. Lim, T. Wang, K. H. Khoo and Z.-K. Tan, Large-Stokes-Shifted Infrared-Emitting InAs–In(Zn)P–ZnSe–ZnS Giant-Shell Quantum Dots by One-Pot Continuous-Injection Synthesis, *Chem. Mater.*, 2019, **31**, 2019–2026.

41 H. Wijaya, D. Darwan, X. Zhao, E. W. Y. Ong, K. R. G. Lim, T. Wang, L. J. Lim, K. H. Khoo and Z. K. Tan, Efficient Near–Infrared Light–Emitting Diodes based on In(Zn)As–In(Zn)P–GaP–ZnS Quantum Dots, *Adv. Funct. Mater.*, 2019, **30**, 1906483.

42 R. Xie, K. Chen, X. Chen and X. Peng, InAs/InP/ZnSe Core/Shell/Shell Quantum Dots as Near-Infrared Emitters: Bright, Narrow-Band, Non-Cadmium Containing, and Biocompatible, *Nano Res.*, 2008, **1**, 457–464.

43 L. K. Sagar, G. Bappi, A. Johnston, B. Chen, P. Todorović, L. Levina, M. I. Saidaminov, F. P. García de Arquer, S. Hoogland and E. H. Sargent, Single-Precursor Intermediate Shelling Enables Bright, Narrow Line Width InAs/InZnP-Based QD Emitters, *Chem. Mater.*, 2020, **32**, 2919–2925.

44 T. G. Kim, D. Zherebetskyy, Y. Bekenstein, M. H. Oh, L. W. Wang, E. Jang and A. P. Alivisatos, Trap Passivation in Indium-Based Quantum Dots through Surface Fluorination: Mechanism and Applications, *ACS Nano*, 2018, **12**, 11529–11540.

45 Y. Kim, J. H. Chang, H. Choi, Y. H. Kim, W. K. Bae and S. Jeong, III-V colloidal nanocrystals: control of covalent surfaces, *Chem. Sci.*, 2019, **11**, 913–922.

46 W. Yang, Y. Yang, A. L. Kaledin, S. He, T. Jin, J. R. McBride and T. Lian, Surface passivation extends single and biexciton lifetimes of InP quantum dots, *Chem. Sci.*, 2020, **11**, 5779–5789.

47 D. G. Kang, Y. H. Won, C. Park, Y. Han and S. K. Kim, The Effect of the Mid–Shell Thickness on the Charge–Carrier Dynamics of the Green–Light Emitting InP/ZnSe/ZnS Core–Shell Quantum Dots, *Adv. Mater. Interfaces*, 2023, **11**, 2300575.

48 K. C. Dümbgen, J. Zito, I. Infante and Z. Hens, Shape, Electronic Structure, and Trap States in Indium Phosphide Quantum Dots, *Chem. Mater.*, 2021, **33**, 6885–6896.

49 M. Kim, M. Choi, S. Choi and S. Jeong, Semiconductor Nanocrystals: Unveiling the Chemistry behind Different Facets, *Acc. Chem. Res.*, 2023, **56**, 1756–1765.

50 J. H. Ko, D. Yoo and Y. H. Kim, Atomic models for anionic ligand passivation of cation-rich surfaces of IV-VI, II-VI, and III-V colloidal quantum dots, *Chem. Commun.*, 2016, **53**, 388–391.

51 J. Hoy, P. J. Morrison, L. K. Steinberg, W. E. Buhro and R. A. Loomis, Excitation Energy Dependence of the Photoluminescence Quantum Yields of Core and Core/Shell Quantum Dots, *J. Phys. Chem. Lett.*, 2013, **4**, 2053–2060.

52 C. Livache, W. D. Kim, H. Jin, O. V. Kozlov, I. Fedin and V. I. Klimov, High-efficiency photoemission from magnetically doped quantum dots driven by multi-step spin-exchange Auger ionization, *Nat. Photonics*, 2022, **16**, 433–440.

53 A. P. Spencer, W. K. Peters, N. R. Neale and D. M. Jonas, Carrier Dynamics and Interactions for Bulklike Photoexcitation of Colloidal Indium Arsenide Quantum Dots, *J. Phys. Chem. C*, 2018, **123**, 848–858.

54 C. Yang, A. Faust, Y. Amit, I. Gdor, U. Banin and S. Ruhman, Impurity Sub-Band in Heavily Cu-Doped InAs Nanocrystal Quantum Dots Detected by Ultrafast Transient Absorption, *J. Phys. Chem. A*, 2016, **120**, 3088–3097.

55 G. Kresse and J. Furthmuller, Efficiency of *ab initio* total energy calculations for metals and semiconductors using a plane-wave basis set, *Comput. Mater. Sci.*, 1996, **6**, 15–50.